https://doi.org/10.22226/2410-3535-2023-1-67-72

Effect of cooling rate on the bainite fraction in low carbon martensitic steel: combined analysis of transformation kinetics and crystal curvature

A. A. Zisman[†,1,2], N. Yu. Zolotorevsky[1], S. N. Petrov[1,2], N. Y. Ermakova[1]

[†]crism_ru@yahoo.co.uk

[1]Peter the Great St.-Petersburg Polytechnic University, St.-Petersburg, 195251, Russia
[2]CRISM "Prometey"-National Research Center "Kurchatov Institute", St.-Petersburg, 191015, Russia

Derived by means of EBSD, statistics of crystal curvature in quenched low carbon steel is analyzed with allowance for its transformation kinetics in terms of dilatometry data. Based on curvature spectra sensitive to the distribution of dislocation density, fractions of martensite and bainite are quantified at high and low cooling rates. Distinction between the resulting microstructures is ascribed to various proportions of their athermal and thermally activated (rate-dependent) constituents.

Keywords: martensite, bainite, transformation kinetics, crystal curvature, EBSD.

1. Introduction

Low carbon martensitic steels are widely used owing to their high strength and fracture toughness combined with good weldability. However, in the case of thick semi-products, the cooling rate and hence the resulting microstructure become rather non-uniform, and a challenging question arises of how this issue will affect the properties of such materials. Depending on the applied quenching, their local volumes contain different fractions of bainite and generally vary in nature of the martensite itself. Its athermal constituent increases with undercooling relative to certain temperature T_{KM} [1]. To assess the latter, no incubation time is suggested, and a temperature dependence of the transformation degree is approximated with an exponential function. Some rate-dependent amount of a new phase may also nucleate slightly above T_{KM} [2–5]. Apart from local variations of microstructure and alloys, this feature is often ascribed to plasticity of austenite that accommodates elastic strains around the martensite embryos and thus facilitates the transformation start. Moreover, fresh dislocations near such crystals serve as further nucleation sites. As far as plasticity in the parent phase is thermally activated, the considered effects intensify in slower cooling, that is, longer exposure to higher temperatures.

When analyzing non-uniformity of steel through thickness, structural elements are characterized by morphological and crystallographic terms. However, *substructures* of freshly transformed crystals should be also allowed for because they may evolve in further cooling. With this issue kept in mind, the present work aims to quantify physically different constituents of the transformed steel dependent on the cooling rate. To this end, the authors will rely on the known regularities derived from relevant data as follows.

Revealed by the up-to-date structural analysis combining various methods [6], coarse martensite laths appear first at former grain boundaries, but growth of such embryos eventually stagnates because plastic accommodation around them is disabled due to the work hardening and decrease of temperature. Then, finer laths form so that the final microstructure consists of two distinguishable fractions. According to [6], the coarse laths are softer, have lower dislocation densities and contain fine carbides. However, in case of slow cooling both lath types undergo the autotempering that weakens their substructural distinction. A remark should be made that the degree of transformation accumulated between its start temperature M_s and $T_{KM} < M_s$ normally does not exceed 15% [2–5]. Therefore, if the most transformation part at a low cooling rate shifts to temperatures above T_{KM}, there is a reason to consider the product phase as a kind of *bainite*. This phase may also form below T_{KM} after some amount of martensite appears [7–11]; however, similar transitions were mostly observed under isothermal conditions rather than in continuous cooling. To facilitate separation of alternative phases, the present paper considers specific (rapid and slow) quenching cases.

Optical microscopy would be irrelevant to the addressed problem because this technique becomes unable to distinguish between structural types coexisting in steel if some of them have relatively low fractions. Let alone artifacts of polishing and etching, the problem aggravates since islands of a minor constituent dispersed among the principal structure are very hard to reveal. Besides, physically different structure types may look *morphologically* similar as, for instance, lath martensite and bainite formed at close temperatures.

Appearance of the EBSD technique [12] has provided a significant advance in analysis of steel microstructures by mapping the crystal orientation and, subsequently, the orientation gradient (crystal curvature). Owing to the

dependence of the latter on dislocation density, curvature maps enable distinction between phases significantly different from this viewpoint (e. g. ferrite, bainite and martensite). Accordingly, some scalar measures for the crystal curvature have been used [13–16] to image and quantify a complex steel constitution in terms of EBSD data. At the same time, regardless of the applied measure, important difficulties still appear in detection of specific low fractions. First, it is not a trivial question of how to predefine certain curvature ranges indicative of various constituents. Second, even if such ranges are somehow selected, discrimination between domains of different structural types is not always accurate because their curvature variations may overlap.

An approach employed in this work to mitigate the above-mentioned limitations is to extract from the treated area a spectrum (overall statistics) of curvature rather than its local values which specify individual elements. According to our experimental results and those earlier reported in [17], *shapes* of such spectra are sufficiently sensitive to small amounts of minor structural types even if their distinction in curvature is not strong. Moreover, such results can be verified by their comparison to the transformation kinetics as provided by dilatometry data.

Among functions applied to map the crystal curvature in terms of the EBSD data [12–16], the most popular ones are KAM (kernel average misorientation) and GAM (grain average misorientation). The former specifies each of periodically arranged data points by an average magnitude of misorientation angles with respect to neighboring points whereas the number of considered coordination layers can be selected by the user. To enhance spatial resolution, we will allow for the first layer only as illustrated in Fig. 1a corresponding to the case of a square grid. However, thus defined KAM depends not only on the bulk lattice curvature but also on orientation jumps across *interfaces*. To avoid related errors, any neighbor with misorientation $\theta > \theta_t$ is excluded according to Fig. 1b where θ_t is a predefined tolerance angle. As to scanning step Δ of EBSD, it should be carefully selected to provide a representative array of data points within any element of the considered structure. Thus, for example, if thickness of martensite laths is about 300 nm, it is advisable to analyze them with $\Delta < 100$ nm. Unlike an essentially local and hence rather noisy KAM, the GAM function is more relevant to *whole* structural elements. It expresses average values of positive KAM over finite domains separated by closed interfaces whereas parameter θ_t to properly draw the latter depends on the specific microstructure. Fig. 1c illustrates the averaging procedure on a virtual scanning line that merges real scanning segments sequentially spaced by Δ. Apparently, higher dislocation densities generating stronger lattice distortions intensify variations of KAM and hence correspond to its higher mean magnitude, that is, GAM. Note that KAM and GAM are expressed in angular units (e. g. degrees) unlike curvature whose physical dimension [angle/length] is relevant to inhomogeneity of elastic lattice rotations. However, at any fixed Δ, as is the case in this work, the considered terms remain proportional to the orientation gradient and hence are suitable in curvature mapping.

Another way to make use of EBSD data on the transformed steel structure is to compare specific interfacial areas between admitted variants of the orientation relationship (OR). As shown in [18,19], statistics of variant coupling is strongly sensitive to the proportion of martensite and bainite. To enhance accuracy, actual rather than virtual reference OR should be used. We will extract them immediately from interfacial disorientations [20,21] thus accelerating computations and excluding errors due to the substructure of prior austenite grains.

The paper is organized as follows. Section 2 represents the considered chemical composition of low carbon steel and describes the employed experimental techniques as well as the numerical approaches to GAM spectra and inter-variant statistics. The results are listed in Section 3 and then briefly discussed in Section 4.

2. Experimental

Chemical composition of the investigated steel (wt.%: 0.09 C, 0.35 Mn, 0.3 Si, 5.5 [Ni+Cu], 1.5 [Mo+Cr], 0.15 V) ensures in its quenched state a mostly martensitic structure for a rather wide range of cooling rates (2 to 80°C/s) covering various industrial conditions. The related CCT diagram has a *single* band-like domain of the transformation whose start and finish temperatures slightly increase at the slower cooling. On the one hand, this effect indicates a deviation from the athermal nature of martensite prescribed by the Koistinen-Marburger equation [1]; it remains a subject of dispute whether this minor feature may be due to the preformed lath bainite. On the other hand, when the diagram provides no certain sign of a *second* phase, its appearance should be verified by an independent method.

Reheated to 950°C and then hold for 100 s, cylindrical specimens (∅5×10 mm) of the considered steel were quenched at cooling rates of 60 and 0.3°C/s on Dil 805-A/D

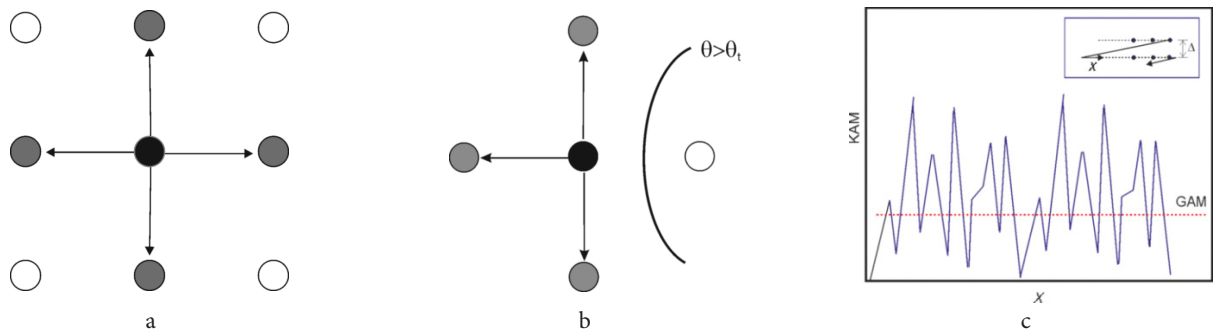

Fig. 1. Next neighbors (gray) of EBSD data point (black) to specify it by KAM in the general case (a) and at an interface (b); determination of GAM by averaging KAM over a whole structural element (c).

dilatometer. The transformation kinetics has been derived from the thermal expansion of specimens. As proposed in [22], to accurately evaluate transformed fractions, the temperature dependence of thermal expansion coefficients is allowed for in both the parent and product phases.

Planar sections were prepared by conventional metallographic procedures and additionally subjected to electrolytic polishing; then the transformed structures have been analyzed by EBSD with a scanning step of 50 nm on SEM Lyra 3-XM at an accelerating voltage of 20 kV. Lattice orientations at discrete data points arranged according to a virtual square grid have been determined within areas of 100 μm in width and height by means of AZTEC software. Depending on OR, the least disorientation between crystal units of martensite should correspond to the minimum *inter-variant* angle. As determined in the considered steel [20], an actual OR close to the Greninger-Troyano relationship is somewhat non-uniform so that the sought parameter varies in the range of 4° to 7°. In the present work we will carefully suggest $\theta_t = 4°$.

To analyze the curvature statistics as discussed in the introduction, the spectra of GAM are extracted from bar charts for its probability density over intervals of 0.02° width. Besides, based on average OR specifically derived for each cooling rate, disorientations for variant couples V_1/V_i $(i = 2, 3, \ldots, 24)$ at randomly selected V_1 have been determined with angular accuracy of one degree to evaluate their frequencies. Along with the transformation kinetics, the revealed character of variant coupling provides independent data to verify results of the curvature analysis. EBSD orientation data were treated with the help of MTEX software.

3. Results

3.1. Transformation kinetics

As shown in Fig. 2 a, at the higher cooling rate the transformation kinetics nicely fits the Koinstinen-Marburger law [1] with $T_{KM} \approx 300$°C except for a minor transformation product appearing at higher temperatures. Note that use of approximate tangent lines neglecting temperature dependences [22] of thermal expansion coefficients would overestimate T_{KM} by about 30°C. An interesting feature of the plot below T_{KM} is a short near-isothermal segment after a notable fraction of athermal martensite has been formed. The related *time* dependence in Fig. 2 b is monotonic so that we can exclude an artifact of dilatometry and admit appearance of bainite. With properties of its isothermal sort [7–11] kept in mind, such an assumption does not seem unlikely. On the one hand, the considered feature appears at the maximum transformation rate; in case of the rapid cooling the latter leads to local adiabatic heating due to an intense release of phase energy. On the other hand, the preformed martensite crystals provide efficient nucleation sites for another phase and local stresses enhancing its formation. To assess an uncertain proportion between bainite and athermal martensite formed *above* T_{KM}, independent data on the curvature distribution are used according to the next section.

In Fig. 2 c for the lower cooling rate about 70% of the transformation takes place above T_{KM} thus evidencing for the formation of bainite then followed by martensite at a sufficient overcooling. Although comparable fractions of such

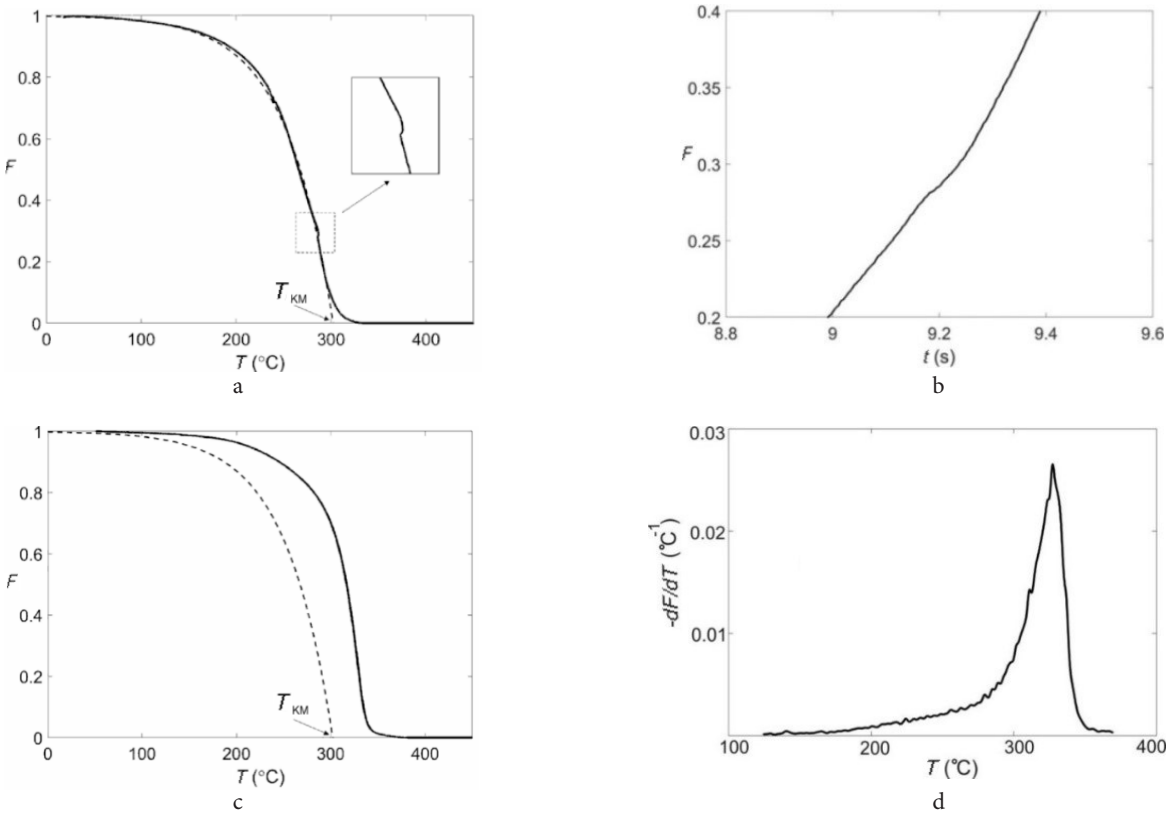

Fig. 2. Transformation kinetics derived from dilatometry data at cooling rates of 60 (a, b) and 0.3°C/s. (c, d). The time dependence in (b) illustrates a gradual formation of bainite, and the derivative plot in (d) displays no distinct sign of alternating phases. The dashed lines correspond to a virtually athermal martensitic transformation, and the insert in (a) zooms in an isothermal stage.

constituents were expected, a rather smooth transformation curve does not enable discrimination between the related stages. This property of the curve is also illustrated by a *mono-modal* distribution of the derivative in Fig. 2 d. One may assume that in the considered case significant amounts of bainite and martensite form *concurrently*; however, further investigations are needed to verify such a development.

3.2. Statistics of crystal curvature

Fig. 3 represents maps of GAM for specimens quenched at cooling rates of 60 and 0.3°C/s. Although the former map displays a somewhat higher *average* level of crystal curvature as expected, distinction between local domains is not strong enough to identify related phase constituents. Instead, as described in Appendix, we will make use of experimental probability density p of GAM further denoted by G. First, a predominant phase is selected according to the transformation kinetics and its contribution to the spectrum of p is approximated by a properly rescaled lognormal function. The latter reflects the physical influence of a current transformation degree on its further rate and has relevant properties (a positive definition range and a longer right tail). This approximation is then subtracted from p to evaluate its constituent due to the minor phase. Specific features of the procedure depend on the cooling rate as follows.

At the high cooling rate, a relatively low fraction of bainite and its weaker curvature should be allowed for. To this end, the main martensite constituent is initially fitted to the *right* tail of experimental p as illustrated in Fig. 4 a. Due to the lowest feature of this tail deviating from the lognormal fitting, the fraction of martensite would be slightly underestimated; that is why a relevant correction by about 3% is then applied. The residual of p involves bainite formed at both $T < T_{KM}$ (a short vertical segment in Fig. 2 a) and at $T \geq T_{KM}$.

Following Appendix again at the low cooling rate (Fig. 4 b), the first appearing bainite constituent is fitted to a part of the *left* tail and its subtraction from p expresses the remaining contribution of martensite. Although fractions of these phases are *roughly* due to the transformation stages above and below T_{KM} (Fig. 2 c), analysis of the crystal curvature distribution may result in a somewhat different proportion as far as both martensite and bainite could partly appear in the transient temperature range.

Table 1 lists the considered phase fractions as evaluated in terms of the transformation kinetics and GAM spectra. Their variations admitted by the former method at the rapid cooling correspond to the above-mentioned uncertainty in constitution of the material fraction transformed above T_{KM}. For the same reason, unlike estimates by EBSD,

Table 1. Fractions (vol.%) of martensite and bainite evaluated by different methods at high and low cooling rates.

Cooling rate, °C/s	Martensite		Bainite	
	Dilatometry	EBSD	Dilatometry	EBSD
60	80 to 93*	81 ± 4	7 to 20*	19 ± 4
0.3	34	38 ± 4	66	62 ± 4

*The martensite-to-bainite ratio at $T > T_{KM}$ is uncertain

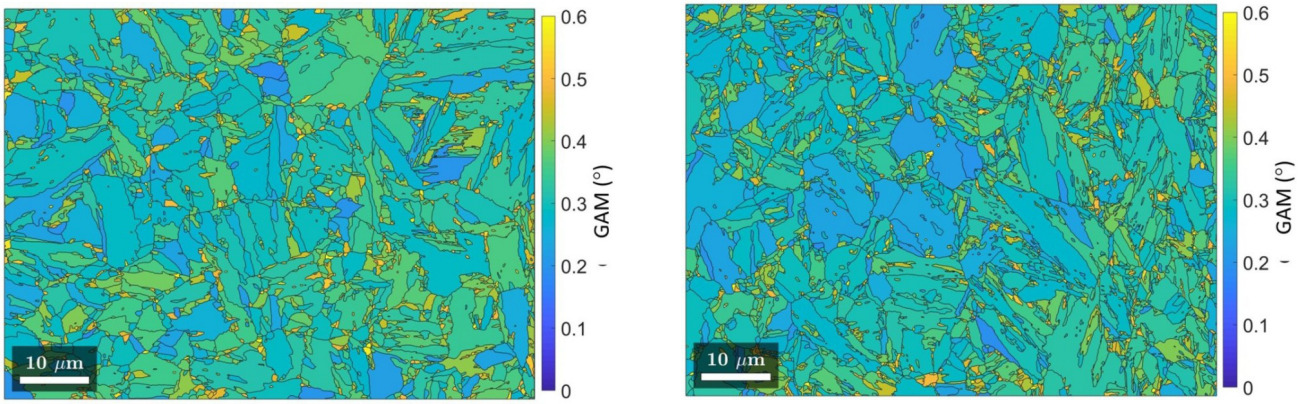

a b

Fig. 3. (Color online) Maps of GAM for specimens quenched at cooling rates of 60 (a) and 0.3°C/s (b).

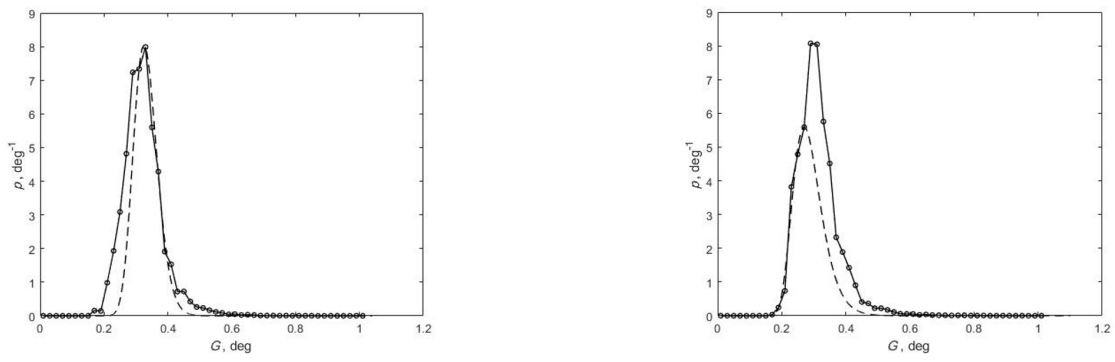

a b

Fig. 4. GAM spectra for specimens quenched at cooling rates of 60 (a) and 0.3°C/s (b). Lognormal functions (dashed lines) fitted to their right and left tails are due to martensite and bainite fractions, respectively.

standard deviations are not indicated. At the low cooling rate, they are also omitted because virtual T_{KM} provides a too rough assessment to be refined by EBSD. Note that the GAM spectrum at the high cooling rate corresponds to the martensite fraction very close to its lower limit as derived from the dilatometry data and thus suggests predominance of bainite in the transformation stage above T_{KM}. Since we investigated *low carbon* steel, this finding complies with the carbon effect recently remarked in [23]. As previously assumed, at the slow cooling the two methods also provide somewhat different results. Specifically, the virtual 66% of bainite attributed to temperatures above T_{KM} in Fig. 2c exceeds 62% resulting from the curvature analysis in terms of EBSD data.

3.3. Coupling of OR variants

According to data on low carbon steels [18], frequency of V_1/V_4 coupling in martensite significantly exceeds that of V_1/V_2 whereas an opposite tendency is characteristic of low-temperature bainite. However, as shown in Fig. 5a, in our case the mostly martensitic structure formed below T_{KM} has a somewhat higher V_1/V_2 fraction indicating some addition of bainite even in the rapid cooling. As expected, this difference increases at the lower cooling rate (Fig. 5b) that enhances the bainite formation. At the same time, it is worth noting that the employed bar charts do not directly express the material fractions occupied by related constituents; indeed, a higher specific *area* of inter-variant boundaries can correspond to smaller crystals coupled in the same *volume*. Although the considered features of variant coupling qualitatively comply with the previous conclusions based on the transformation kinetics and the distribution of crystal curvature, an unexpected predominance of V_1/V_2 in Fig. 5a deserves some discussion. In the authors' opinion, this is due to $T_{KM} \approx 300$°C of our steel, alloyed by Ni that is about 130°C lesser with respect to low carbon steel considered in [18]. This overcooling promotes the self-accommodation of lath packets affecting their structure. Accordingly, as shown in the case of medium carbon martensite [19], the *reference* variant coupling proposed in [18] should be adjusted to specific M_s dependent on the chemical composition of steel.

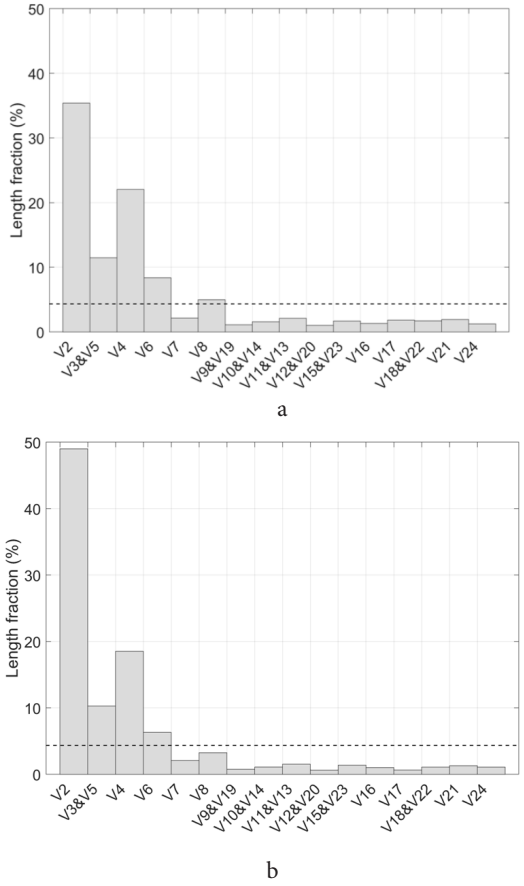

Fig. 5. Statistics of OR variant coupling at cooling rates of 60 (a) and 0.3°C/s (b). Dotted lines show the level for random coupling.

4. Concluding remarks

According to the reported results, mutually complementary data on the transformation kinetics by dilatometry and the distribution of lattice curvature by EBSD enable quantification of the bainite fraction in low carbon martensitic steel as follows.

In case of high cooling rate, the transformation kinetics indicates a small fraction of bainite nucleated below temperature T_{KM} after a significant fraction of athermal martensite. The bainite formation following some amount of preformed martensite was already registered under isothermal conditions [7–11] or in the decelerated cooling [24]; however, to the authors' knowledge, such a development has never been noted in the rapid quenching. According to the same transformation curve, some minor mixture of bainite and martensite forms at $T_{KM} < T < M_s$ although their proportion remains uncertain. Predominance of bainite in this range has been revealed in terms of the crystal curvature. However, discrimination between the two constituents of lath morphology formed at close temperatures remains somewhat formal since their dislocation densities are also almost similar [25].

At the low cooling rate, a smooth transformation curve mostly due to $T > T_{KM}$ has no distinct sign of the bainite-to-martensite transition so that statistics of the crystal curvature becomes indispensable. As expected, this indicates a drift of the whole GAM spectrum to left whereas analysis of its shape suggests comparable fractions of the two phases; at the same time, the question persists of whether they have been formed concurrently or sequentially. Moreover, stronger overlapping of their curvature ranges at *intermediate* cooling rates will necessitate use of some independent data as, for example, local crystallographic textures [26].

Appendix

Let p be probability density for an experimental sampling of G and its components q_B and q_M due to bainite and martensite, respectively, should be derived from the spectrum of p. To this end, a *predominant* phase is selected first according to the transformation kinetics (Fig. 2) and the respective component is then approximated by a continuous function with allowance for the spectrum shape. Thereafter, another component is found by subtraction of this approximation

from p. The considered function for q_B or q_M is sought in a form

$$W = \alpha w \quad 0 < \alpha < 1 \qquad (1)$$

where

$$w = (2\pi)^{-1/2}(G\sigma)^{-1}\exp\{-(Ln(G)-\mu)^2/(2\sigma^2)\} \qquad (2)$$

is the lognormal function determined by parameters μ and σ. It was necessary to rescale w since its integral over axis G reaches unity that apparently exceeds an integral of whatever *constituent* W.

Parameters μ, σ and α are sought to get

$$\Sigma_{i=m}^{n}(F_i - p_i)^2 = \min \qquad (3)$$

over a specific part of experimental p spectrum (sequence of G intervals $m \le i \le n$). At the higher cooling rate (Fig. 4 a) resulting in predominant martensite, $W = q_M$ is fitted to the *right* tail of p. At the lower cooling rate (Fig. 4 b) the fitting of $W = q_B$ due to bainite involves a part of the *left* tail of p preceding an inflection point before its main peak. Although the nonlinear least-square method is employed in each case to find three parameters (μ, σ and α), there are only *two* degrees of freedom since the median of any W is *fixed* at that of p and hence imposes one more constraint. Finally, an integral of W expresses the predominant phase fraction whereas its subtraction from unity provides a residual fraction due to another phase.

Acknowledgements. The authors acknowledge a financial support of this work by the Russian Science Foundation, project No 22-19-00627.

References

1. D. P. Koistinen, R. E. Marburger. Acta Metall. 7, 59 (1959). Crossref
2. K. Jeyabalan, S. D. Catteau, J. Teixeira, G. Geandier, B. Denand, J. Dulc, S. Denis, G. Michel, M. Courteaux. Materialia. 9, 100582 (2020). Crossref
3. S. Ramesh Babu, D. Ivanov, D. Porter. ISIJ Int. 59, 169 (2019). Crossref
4. J. R. C. Guimarães, P. R. Rios. J. Mater. Res. Technol. 7, 499 (2018). Crossref
5. S. M. C. van Bohemen, J. Sietsma. Mater. Sci. Technol. 30, 1024 (2014). Crossref
6. L. Morsdorf, C. C. Tasan, D. Ponge, D. Raabe. Acta Mater. 95, 366 (2015). Crossref
7. Z. Wei, H. Hu, M. Liu, J. Tian, G. Xu. Metals. 12(1), 104 (2022). Crossref
8. L. Qian, Z. Li, T. Wang, D. Li, F. Zhang, J. Meng. J. Mater. Sci. Technol. 96, 69 (2022). Crossref
9. C. Rampelberg, S. Y. P. Allain, G. Geandier, J. Teixeria, F. Lebel, T. Sourmail. JOM. 73, 3181 (2021). Crossref
10. S. Samanta, P. Biswas, S. B. Singh. Scripta Mater. 136, 132 (2017). Crossref
11. A. Navarro-Lopez, J. Sietsma, M. J. Santofimia. Metall. Mater. Trans. A47, 1028 (2016). Crossref
12. B. L. Adams, S. I. Wright, K. Kunze. Metall. Trans. A24, 819 (1993). Crossref
13. S. I. Wright, M. M. Nowell, D. P. Field. Microsc. Microanal. 17, 316 (2011). Crossref
14. R. F. Tomaz, D. B. Santos, K. Camey, R. Barbosa, M. S. Andrade, D. P. Escobar. J. Mater. Res. Technol. 8, 2423 (2019). Crossref
15. A. A. Gazder, F. Al-Harbi, Y. T. Spanke, D. R. G. Mitchel, E. V. Pereloma. Ultramicr. 147, 114 (2014). Crossref
16. S. Breumier, T. Martinez Ostormujof, B. Frincu, N. Gey, A. Couturier, N. Loukachenko, P. E. Aba-perea, L. Germain. Mater. Char. 186, 111805 (2022). Crossref
17. A. A. Zisman, N. Yu. Zolotorevsky, S. N. Petrov, E. I. Khlusova, E. A. Yashina. Metal Sci. Heat Treat. 60, 142 (2018). Crossref
18. N. Takayama, G. Miyamoto, T. Furuhara. Acta Mater. 60, 2387 (2012). Crossref
19. A. Stormvinter, G. Miyamoto, T. Furuhara, P. Hedstroem, A. Borgenstam. Acta Mater. 60, 7265 (2012). Crossref
20. N. Y. Zolotorevsky, S. N. Panpurin, A. A. Zisman, S. N. Petrov. Mater. Charact. 107, 278 (2015). Crossref
21. T. Nyyssonen, P. Peura, V. T. Kuokkala. Metall. Mater. Trans. A49, 6246 (2018). Crossref
22. S. Choi. Mater. Sci. Eng. A. 363, 72 (2003). Crossref
23. S. Dhara, S. M. C. van Bohemen, M. J. Santofimia. Mater. Today Comm. 33, 104567 (2022). Crossref
24. X. Zhang, H. Yu, Q. Li, C. Song, S. Yang. Mater. Sci. Eng. A840, 142968 (2022). Crossref
25. M. Takahashi, H. K. D. Bhadeshia. Mater. Sci. Technol. 6, 592 – 603 (1990). Crossref
26. A. A. Zisman, N. Yu. Zolotorevsky, S. N. Petrov, E. I. Khlusova, E. A. Yashina. Inorg. Mater.: Appl. Res. 12, 1521 (2021). Crossref